IET Power Electronics

WILEY

The Institution of Engineering and Technology

ORIGINAL RESEARCH OPEN ACCESS

Hardware Test and Validation of the Angular Droop Control: Analysis and Experiments

Taouba Jouini[1,2] | Jan Wachter[2] | Sophie An[2] | Veit Hagenmeyer[2]

[1]Institute of Automatic Control, Leibniz University of Hannover, Hannover, Germany | [2]Institute for Automation and Applied Informatics, Karlsruhe Institute of Technology, Karlsruhe, Germany

Correspondence: Jan Wachter (jan.wachter@kit.edu)

Received: 11 September 2025 | **Revised:** 16 December 2025 | **Accepted:** 23 February 2026

ABSTRACT

We present a hardware-based validation of angular droop control for grid-forming DC/AC converters, a control strategy that establishes active power-to-angle droop. Angular droop control enables exact frequency regulation at steady state, thereby combining primary and secondary control into a single layer. We provide traceable analysis and suggest solutions to the main implementation challenges with angular droop control, specifically addressing the challenges concerning discretization and clock drift in hardware experiments. This is illustrated in two different scenarios. Experimental results from the single converter to load scenario demonstrate black start capability and power-to-angle droop behavior for two different implementation schemes. A multi-converter setup validates frequency synchronization and power-sharing properties, proving the ancillary services that angular droop control provides in the real-world experimental setup.

1 | Introduction

Power grids are facing a rapid transition from fossil fuel towards an increasing share of renewable energy resources. This profound change is characterized by the integration of converter-based generation [1]. In particular, the high penetration of power electronics alters the power system dynamics, governed thus far by rotating synchronous machines underpinning the legacy grid [2]. Therefore, the control of DC/AC converters lies at the forefront of this transition to ensure power system stability [3].

Typical control approaches for grid-forming DC/AC converters are inspired by the dynamics governing synchronous machines and their analogy to coupled oscillator dynamics [4]. For example, *frequency droop* control is based on the active power to frequency droop, which is inherent to synchronous machines and enables the synchronization between different generators. This grid-forming method is extensively studied both in theory and practice. An experimental validation of the frequency droop control strategy for different applications can be found in [5]. The dynamics of synchronous machines remain a source of inspiration for a multitude of converter control strategies that emulate their behavior. One particular controller that relies on exact model matching of high-order dynamics of synchronous machines is the *matching control* introduced in [6, 7]. This controller relies on easily measured DC-side voltage to play the role of an indicator of power imbalance in the grid. Oscillator-based control schemes such as the *virtual oscillator control* [8] rely on emulating the dynamics of weakly coupled nonlinear oscillators. Compared to frequency droop control, which is only well-defined in the vicinity of a sinusoidal steady state, virtual oscillator control enables interconnected converters to stabilize synchronous sinusoidal waveforms starting from arbitrary initial condition. The virtual oscillator control is validated experimentally in [9] within a laboratory hardware prototype to demonstrate the validity of the design approach. Even though the virtual

The first two authors contributed equally to this article.

oscillator control has provable active power to frequency droop properties [10], the control tuning remains a difficult task due to a lack of intuition on the physical interpretation of the gains. It was also not possible to track active and reactive power setpoints in its original formulation in [8]. These limitations have motivated a variant of virtual oscillator control suggested in [11] that allows active and reactive power to be dispatched, hence the name *dispatchable virtual oscillator control* whose experimental validation is conducted in [12]. The authors in [13] design an angle based modification for a frequency droop controller to dampen power oscillations in a multiple converter setup.

All the control approaches discussed above have in common that they are based on the principle of active power to frequency droop. In contrast, the *angular droop* control studied in this paper establishes a linear relationship between active power and angle deviation, rather than frequency. This achieves exact frequency regulation at steady state. As a consequence, it merges primary with secondary frequency control [14] and no additional control layer, that is, secondary control is necessary. During transients, compared to frequency droop control, the angular droop acts on the rate of change of frequency to counterbalance the rate of change of power which anticipates a change in the power balance itself. Therefore angular droop control reacts faster to load disturbances. Additionally, the angular droop control is shown to be inverse optimal stabilizing for the angle dynamics [15, 16]. The optimality of the angular droop control brings about inherent desirable gain margins analogous to linear quadratic regulators and showcases the utility of inverse optimal control theory in networked settings [17]. Angular droop control has been tested in simulations on numerous power system benchmarks. In [14] the operation of a simulated microgrid consisting of angular droop controlled DC/AC converters is presented and the zero frequency deviation property at steady state is shown in comparison to frequency droop control. Kolluri et al. [18] examine the power sharing properties of angular droop control and validate their results using a simulation study. Xu et al. [19] deploy a simulation study of an islanded microgrid to validate an angular droop based method for cost minimization and consensus active power sharing between distributed generation units. In [15], it is proven that angular droop is an inverse optimal locally stabilizing control law for a multi-converter system, which is supported by numerical simulations. Those results are extended [20] to account for input and output constraints posed by real-world applications and the tuning of discrete-time implementations of angular droop control is discussed in [21]. Both studies support their results using numerical simulations.

The sole deployment of numerical simulations for validation is unsatisfactory due to the discrepancy between real-world setups and simplified settings adopted in numerical case studies such as unmodeled dynamics and erroneous or unknown model parameters affecting the system.

This work demonstrates the grid-forming properties of angular droop control in a controlled experimental setting [22], with particular emphasis on the hardware-based validation. The main contributions are as follows:

- This paper presents the first hardware-based implementation of angular droop control. The challenges of opting for angle- instead of frequency-based control are addressed in a real hardware experimental setup.
- Grid-forming properties such as black start, robustness to load changes, and zero steady state frequency deviation property of angular droop control are validated using the single converter-to-load scenario. The control law is reformulated to suit hardware realization, and two implementation schemes are compared to show compatibility with different inner control architectures.
- Frequency synchronization and power-sharing capabilities are proven in the two-converter scenario, forming the basis for generalization to n-converter setups. Clock drift issues are analyzed and mitigated via master clock distribution. Further, practical guidance on control tuning for angular droop is provided.

This experimental validation represents a meaningful contribution toward the practical deployment of angular droop control, helping to bridge the gap between theoretical development and real-world implementation.

The paper is structured as follows. Section 2 first briefly introduces angular droop control and discusses the difference to frequency droop control, then details the experimental environment. Thereafter, in Section 2.4 the results of the single converter to load scenario are discussed along with the challenge of discretizing the angle dynamics. Section 3 is concerned with the two-converter to load scenario and the challenges connected to synchronization and power-sharing. Lastly, Section 4 summarizes the findings and concludes the paper.

Notation. Define $\mathbf{I} = \left[\begin{smallmatrix} 1 & 0 \\ 0 & 1 \end{smallmatrix}\right]$ and $\mathbf{J} = \left[\begin{smallmatrix} 0 & -1 \\ 1 & 0 \end{smallmatrix}\right]$. Let x denote an AC quantity in abc-frame and $x_{dq} := \mathcal{P}(\theta_{dq})x$ denote its transformation in dq-frame [23] following a Park transformation $\mathcal{P}(\theta_{dq})$ with angle $\theta_{dq}(t) := \theta_k(t)$, where θ_k is the angle of converter k. Consider a network described by a connected graph $\mathcal{G} = (\mathcal{V}, \mathcal{E}, \Xi)$, consisting of $|\mathcal{V}| = n$ nodes representing DC/AC converter buses and $|\mathcal{E}| = m$ edges modeling purely inductive transmission lines with susceptance $b_{kj} > 0$, $(k, j) \in \mathcal{E}$ collected in the diagonal matrix $\Xi = \mathrm{diag}(b_{kj})$, $(k, j) \in \mathcal{E}$. The topology of the graph $\mathcal{G}$ is described by the incidence matrix $\mathcal{B} \in \mathbb{R}^{n\times m}$.

2 | The Angular Droop Control

2.1 | Control Scheme

Consider a network of DC/AC converters, each represented by a voltage phasor. Hereby all the phasors are modeled with a constant magnitude (e.g., one per unit), and the converter's angle dynamics are assumed to be controllable. Overall the network dynamics can be represented by,

$$\dot{\theta} = \hat{u}(\theta) + \omega^* \mathbb{1}_n, \quad \theta(0) = \theta_0, \tag{1}$$

where $\hat{u}(\theta) = [\hat{u}_1(\theta), \ldots, \hat{u}_n(\theta)]^\top \in \mathbb{R}^n$ is the main control input, $\theta = [\theta_1, \ldots, \theta_n]^\top \in \mathbb{R}^n$ is the vector of phase angles of the DC/AC converters, $\theta_0 = [\theta_{0,1}, \ldots, \theta_{0,n}]^\top \in \mathbb{R}^n$ is the initial angle vector and ω^* is the nominal angular frequency. The angular droop

control is given by [15, 16],

$$\hat{u}(\theta) = -\frac{1}{2}R^{-1}\left(\Gamma\left(\theta - \theta^*\right) + P(\theta) - P^*\right), \tag{2}$$

with $R = \mathrm{diag}(\alpha_1, \ldots, \alpha_n) > 0$, $\Gamma = \mathrm{diag}(\gamma_1, \ldots, \gamma_n) > 0$. Further, $P(\theta) = [P_1(\theta), \ldots, P_n(\theta)]^\top \in \mathbb{R}^n$ denotes the active power vector, and $\theta^* = [\theta_1^*, \ldots, \theta_n^*]^\top \in \mathbb{R}^n$ and $P^* = [P_1^*(\theta), \ldots, P_n^*(\theta)]^\top \in \mathbb{R}^n$ the respective reference values. Note that for the angular droop control design (2), we assume that synchrophasor measurements of the angle, with respect to a global frame of reference, are available to each converter. This is a reasonable scenario for a future power grid, as phasor measurement unit (PMU) installation is becoming increasingly widespread [24–26]. In summary, the closed-loop angle dynamics are given by,

$$\dot{\theta} = -\frac{1}{2\alpha}(\gamma\left(\theta - \theta^*\right) + P(\theta) - P^*) + \omega^* \mathbb{1}_n, \tag{3}$$

where the gain matrices $R = \alpha\, \mathbf{I}_n$ and $\Gamma = \gamma\, \mathbf{I}_n$ with $\alpha, \gamma > 0$, that is, the control gains are uniform across all the converters. Observe that:

- A decrease in the gain $\alpha > 0$ improves the angle transients, that is, it results in faster convergence of the angles towards the induced steady state angle.
- The gain $\gamma > 0$ defines the power-to-angle droop behavior between the power and angle deviation at steady state characterized by

$$\Gamma\left(\theta^s - \theta^*\right) = P^* - P^s(\theta^s), \tag{4}$$

  where $\theta^s \in \mathbb{R}^n$ and $P^s(\theta^s)$ are the vectors of induced steady state angles and powers, respectively.
- Both the gains γ and α affect the rate of change of frequency or RoCoF given by $\dot{\omega}$. This can be seen by taking the time derivative of (3) as follows

$$\ddot{\theta} = -\frac{1}{2\alpha}\Big(\gamma(\dot{\theta} - \dot{\theta}^*) + \dot{P}(\theta)\Big), \tag{5}$$

  where $\dot{P}(\theta) = \frac{\mathrm{d}P(\theta)}{\mathrm{d}t}$. By letting $\omega := \dot{\theta}$ and $\omega^* := \dot{\theta}^*$, we have

$$\dot{\omega} = -\frac{1}{2\alpha}\left(\gamma\left(\omega - \omega^*\right) + \dot{P}(\theta)\right). \tag{6}$$

  Therefore, a sudden change in active power corresponds to a sudden RoCoF $\dot{\omega}$ that occurs during the transients, while the frequency error remains zero at steady state. Observe that the RoCoF depends on both gains α and γ.

2.1.1 | Stability and Optimality

For clarity of exposition, we introduce the error coordinates $\tilde{\theta}(t) = \theta(t) - \theta^*(t)$, the angle vector at induced steady state $\theta^s := \lim_{t\to\infty} \theta(t)$ and consider the following optimal control problem [15],

$$\min_{u\in\mathbb{R}^n} \int_0^\infty \sum_{k=1}^n \left(\alpha_k u_k^2(\tilde{\theta}) + \frac{1}{4\alpha_k}\left(\gamma_k \tilde{\theta}_k + P_k(\tilde{\theta}) - P_k^*\right)^2\right) \mathrm{d}t,$$
$$\text{s.t. } \dot{\tilde{\theta}} = \hat{u}(\tilde{\theta}), \quad \tilde{\theta}(0) = \tilde{\theta}_0. \tag{7}$$

Assumption 1 [15]. The induced steady state angle vector $\tilde{\theta}^s = \{\tilde{\theta}_k^s\}_{k=1}^n$ satisfies, $\mathcal{B}^\top \tilde{\theta}^s \in \left(-\frac{\pi}{2}, \frac{\pi}{2}\right)^m$, where $\mathcal{B} \in \mathbb{R}^{n\times m}$ is the incidence matrix of the underlying graph $\mathcal{G}$.

Under Assumption 1, the angular droop control is the optimal stabilizing solution of (7) in a neighborhood of the induced steady state angle $\tilde{\theta}^s$ that satisfies

$$\Gamma\, \tilde{\theta}^s = P^* - P^s(\tilde{\theta}^s), \tag{8}$$

where $P^s(\tilde{\theta}^s) = [P_1^s(\tilde{\theta}^s), \ldots, P_n^s(\tilde{\theta}^s)]^\top$ is vector of the induced steady state active power [15]. Note that (8) describes the steady state as a power balance between the active power and angle deviation from the nominal value. It coincides with the steady state resulting from letting the running cost in (7) go asymptotically to zero, that is,

$$\lim_{t\to\infty}\left(\gamma_k \tilde{\theta}_k(t) + P_k(\tilde{\theta}(t)) - P_k^*\right) = 0, \quad \forall\, k = 1, \ldots, n.$$

2.2 | Angular vs. Frequency Droop—Distinction of Properties

In this section, we highlight the merits of the angular droop control compared to frequency droop control in terms of frequency support and steady state behavior. In particular, we provide a comprehensive analysis that demonstrates why angular droop advances the state-of-the art.

Inspired by the dynamics governing synchronous machines and their analogy to coupled oscillator dynamics [4], frequency droop control is a grid-forming method that obeys the following closed-loop dynamics:

$$\dot{\omega} = -\frac{1}{2\alpha}(\gamma\left(\omega - \omega^*\right) + P(\theta) - P^*). \tag{9}$$

For easiness of comparison, we hereby denote the virtual inertia $M = 2\,\alpha\, \mathbf{I}_n$ and the damping coefficient $D = \gamma\, \mathbf{I}_n$.

Linking active power to angle instead of frequency yields altogether different behavior during both transient and steady state, by comparing the frequency droop dynamics (9) to angular droop dynamics (3), we observe that:

2.2.1 | Frequency Support

For the angular droop control, the rate of change of frequency or RoCoF is induced by the rate of change of power in (6) and not the power imbalance itself as in (9). This means that the angular droop acts on the rate of change of frequency to counterbalance the rate of change of power which anticipates a change in the power balance itself. This is analogue to a derivative control that extrapolates the current slope of the error and generates one large corrective effort immediately after a load change in order to begin eliminating the error as quickly as possible. A loop with derivative control recovers quicker from a disturbance with less deviation than a loop with only a proportional term as in frequency droop control.

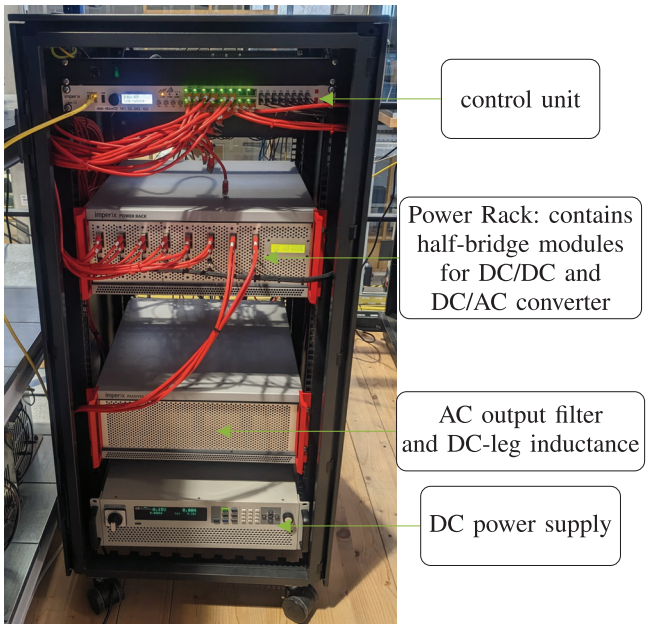

FIGURE 1 | Overview of a programmable DC/AC converter system for the hardware experiments.

2.2.2 | Steady State Behavior

At steady state, the frequency droop behavior established by (9) is given by

$$\gamma\,(\omega^s - \omega^*) = P^* - P(\theta^s). \tag{10}$$

Here, the induced steady state frequency ω^s deviates from the nominal frequency ω^* and depends directly on the magnitude of the disturbance affecting the power network. Therefore a secondary control is necessary to bring the steady state frequency back to nominal. On the other hand, the steady state frequency induced by angular droop control, see (8), settles to its nominal value at steady state in disregard of the disturbance amplitude implying *zero* frequency error and thus merging primary and secondary control [14]. Please refer to Figure 9 in Section 2.7 for the experimental results on this comparison. This saves additional control effort while achieving the same result.

2.3 | Experimental Setup

The hardware testbed consists of programmable DC/AC converter systems, a resistive load and transmission line replicas. Relevant parameters of the setup are summarized in Table 1. Details about the model under consideration are presented in Appendix A. For further information on the microgrid laboratory refer to [22].

As shown in Figure 1, the hardware representation of the programmable DC/AC converter system consists of a DC power supply, DC/DC converter, a control unit, a DC/AC converter and an output filter.

TABLE 1 | Technical details of the hardware setup.

DC/AC converter and its control		
Symbol	**Definition**	**Value (S.I.)**
V^*	AC voltage amplitude	$230\sqrt{2}$
C	AC filter capacitance	$1 \cdot 10^{-5}$
L	AC filter inductance	$2.36 \cdot 10^{-3}$
R	AC filter resistance	$1 \cdot 10^{-3}$
G	Load resistance	58.77
V_{dc}	DC-link voltage	750
f_{sw}	Switching frequency	20 kHz
A	Modulation amplitude	0.8132
Angular droop control		
Symbol	**Definition**	**Value (S.I.)**
P^*	Nominal active power	2880
ω^*	Nominal angular frequency	$2\pi 50$
α	Input effort gain	2000
γ	Steady state gain	$5 \cdot 10^4$
k_{VP}	P-voltage gain	0.05
k_{VI}	I-voltage gain	0.4
k_{IP}	P-current gain	10
k_{II}	I-current gain	240
Parameters values of the transmission line		
Symbol	**Definition**	**Value in S.I.**
R_l	Line resistance	$20 \cdot 10^{-3}$
L_l	Line inductance	$700 \cdot 10^{-6}$

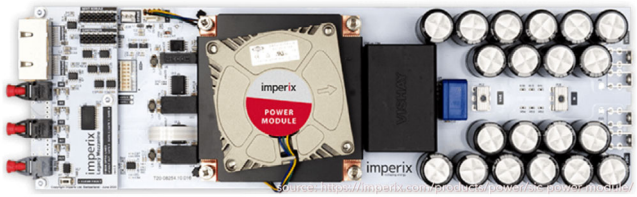

FIGURE 2 | Exemplary image of the half-bridge modules [27] contained in the power rack.

2.3.1 | Programmable DC/AC Converter System

- DC Power Supply: emulates the power source of the DC/AC converter system and has a rated power of 15 kW.
- DC/DC Converter: consists of a boost converter which is build using a half-bridge module [27] as well as an inductance of $L_b = 1.3$ mH. The system is controlled to regulate the DC bus voltage at the desired value.
- DC/AC Converter and Output Filter: the two-level three-phase DC/AC converter system consists of SiC-MOSFET half-bridge modules, see Figure 2, including an embedded

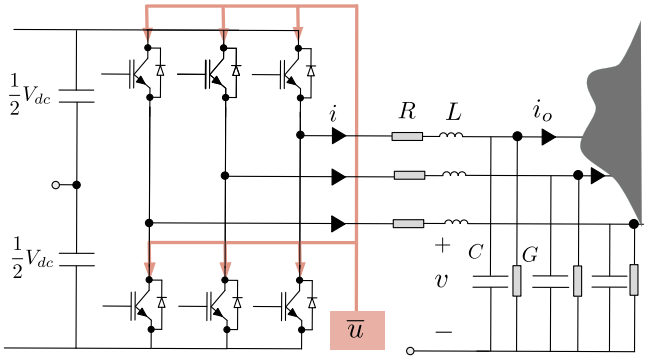

FIGURE 3 | A three-phase DC/AC converter model under study. Each phase-leg consists of a half-bridge module [27]. The modulation input $\bar{u}$ is obtained either directly (direct control) or via well-known cascaded voltage and current control (indirect control), for control diagrams and further details see Appendix A.

DC-bus of 500 μF, as described in [27]. To form the three-phase DC/AC converter, the half-bridge modules are connected on the DC-side to form a common DC-bus, which is supplied by the DC/DC converter with a constant voltage. The output filter consists of an inductance in series with a parasitic resistance for each of the phases. They are set in parallel with a capacitance to form a LC-filter [28]. The DC/AC converter system has a rated power of $P_{rated} = 15$ kW and a nominal voltage of $230\sqrt{2}$ V. The schematics are shown in Figure 3.

- Control Unit: the real-time control unit [29] executes the user code and controls both the DC/DC and the DC/AC stage during the experiments. The control cycle frequency of 20 kHz is well above the nominal grid frequency of 50 Hz such that the control latency has only negligible effect on the presented results.
- Measurement Sensors: To obtain the necessary measurements for the control of the converters and presentation of the results, the following sensors are used:
  - Current Sensors [30]: the measurement range of ±50 A is well suited for this application and the bandwidth of 200 kHz is large enough to cover the relevant frequency range, considering a switching frequency of 20 kHz and nominal grid frequency of 50 Hz. Further, the typical sensitivity error of the sensors is ±0.4% which is sufficient for the control usecase. The input-referred noise is 0.05 A, which is several orders of magnitude smaller than the operating point during the experiments and therefore has negligible effect on the presented results.
  - Voltage Sensors [31]: the measurement range of ±800 V and the bandwidth of 100 kHz is sufficient to capture the relevant dynamics, considering the switching frequency of 20 kHz and nominal grid frequency of 50 Hz. Further, the typical sensitivity error of the sensors is ±0.35 % which is adequate for the control usecase. The input-referred noise is 1.4 V, which is sufficiently small compared to the operating voltage.

  Since each phase voltages and currents are obtained by individual sensors, the values for the sensitivity and offset differ slightly even after calibration. Such sensor-specific errors can lead to an imbalance in the measured phase currents and voltages, which generates inter-harmonic components in derived values such as the active power.

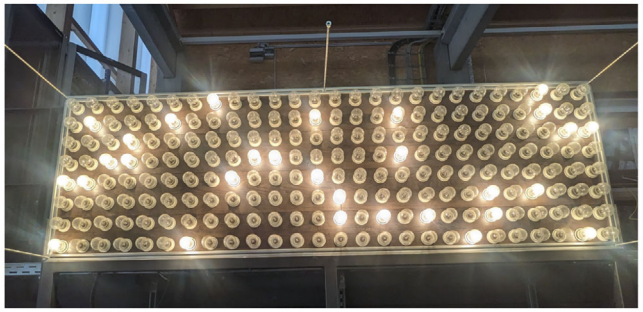

FIGURE 4 | Resistive load represented by incandescent light bulbs.

The parameter values of the programmable DC/AC converter are summarized in Table 1.

2.3.2 | Resistive Load

We consider a light-wall to represent a resistive load, see Figure 4. Each of the light bulbs has a power consumption of 100 W at nominal voltage of $230\sqrt{2}$ V and can be individually controlled via a programmable logic controller to set the desired power consumption.

2.3.3 | Transmission Line Replica

The physical transmission line properties are emulated using resistive and inductive type line replicas. Discrete hardware elements are connected in series to provide the desired physical quantities in order to replicate the effect of a given length and type of transmission line [22], see Figure 5. The parameter values of the transmission line of our experimental setup are given in Table 1.

2.4 | Scenario I: Single Converter to Load

Angular droop control operates in a different domain than conventional frequency droop by linking active power to angle rather than frequency. Although angle and frequency are related through integration, this distinction poses challenges for the real-world implementation.

2.5 | Scenario Goals and Description

To experimentally verify the properties of the angular droop hardware implementation under real-world conditions, we start with Scenario I: a single DC/AC converter system in closed-loop with the angular droop control is connected to a resistive load, as shown in Figure 6.

With Scenario I we show:

- black start capabilities, namely the ability to form sinusoidal wave after a major event, for example, a blackout.

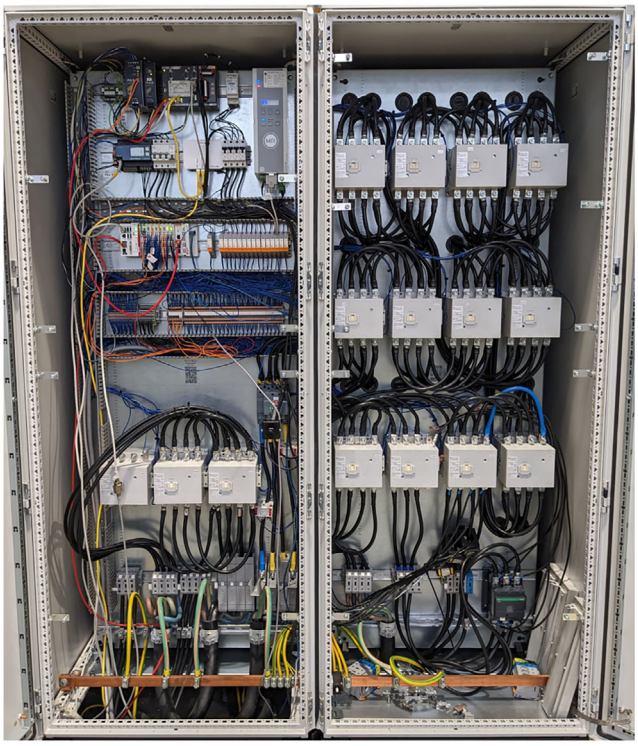

FIGURE 5 | Transmission line replica in our experimental setup.

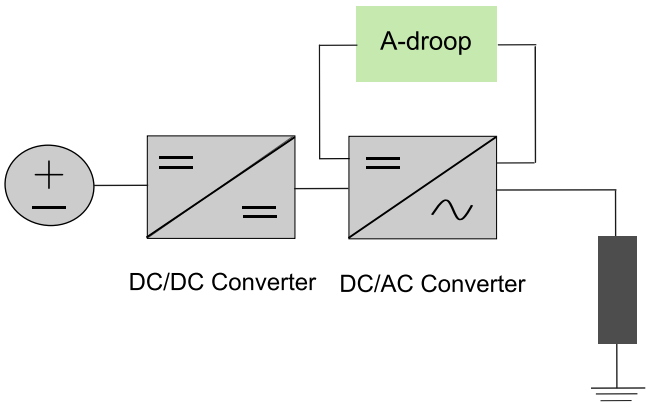

FIGURE 6 | Schematic representation of Scenario I consisting of a balanced three-phase DC/AC converter in closed-loop with angular droop control and connected to a resistive load.

- the capability to withstand load disturbance, for example, upon a sudden increase/decrease in the load power.
- influence of direct and indirect implementation schemes on the angular droop behavior and drawing a comparison between them. The modulation input $\bar{u}$ of the DC/AC converter is obtained either directly (direct control) or via well-known cascaded voltage and current control (indirect control), details see in Appendix A.

The single-converter test case is crucial for assessing the resilience of the closed-loop converter system against disturbances of varying magnitudes. The ability to withstand small to medium disturbances is particularly relevant in conditions close to nominal operation, while grid-forming capabilities become essential following major disruptions such as blackouts. Comparing direct and indirect implementations shows the compatibility of angular droop with well established control architectures, while preserving its properties.

2.6 | Challenge: Discretization of the Angle Dynamics

2.6.1 | Analysis

The angular droop control described in Section 2, also see Appendix A, needs to conform with the restrictions posed by real hardware, in particular its implementation in discrete-time. For this, we discretize the closed-loop angle dynamics in (3) using the forward Euler method as follows,

$$\theta(s+1) = \theta(s) + T_s\, u_d(s) + \omega^* \mathbb{1}_n\,, \tag{11}$$

$$u_d(s) = -\frac{1}{2} R^{-1} \left(\Gamma\left(\theta(s) - \theta^*(s)\right) + P(\theta(s)) - P^*\right),$$

where $s \in \mathbb{Z}$ is the time step, $T_s > 0$ is the sampling period and $\omega^* > 0$ is the nominal angular frequency. Next, we define the angle error coordinate $\Delta\theta(s) = \theta(s) - \theta^*(s)$ where $\theta^* \in \mathbb{R}^n$ denotes the nominal angle satisfying

$$\theta^*(s+1) = \theta^*(s) + T_s\, \omega^*. \tag{12}$$

From (11), the discrete-time angle error dynamics are given by,

$$\Delta\theta(s+1) = \Delta\theta(s) - \frac{1}{2} T_s\, R^{-1} \left(\Gamma \Delta\theta(s) + P(\theta(s)) - P^*\right). \tag{13}$$

Observe that in (12), the nominal steady state angle vector θ^* grows infinitely. This causes a loss of precision for the stored variable $\theta(s)$ due to the limit of available bytes for single precision.

2.6.2 | Proposed Solution

The previous observation motivates the following solution. We aim to find a mapping of the angles θ^* from $\mathbb{R}^n$ to the n-th dimensional torus $\mathbb{T}^n$. Note that the sine function appearing in the implementation of the modulation signal $\bar{u}$ both for the direct (A3) and indirect (A4) schemes is 2π periodic in the angle $\theta(s)$. We proceed by limiting the values of the nominal angle $\theta^*(s)$ as follows,

$$\theta^*(s+1) = \theta^*(s) + T_s\, \omega^* (\mathrm{mod}\, 2\pi), \tag{14}$$

which yields the following absolute angles,

$$\theta(s+1) = \theta^*(s+1) + \Delta\theta(s+1). \tag{15}$$

Here, $\Delta\theta(s+1)$ is given by (13). Therefore the angles $\theta(s)$, $s \in \mathbb{Z}$ remains within feasible numerical bounds. Our proposed solution optimizes the space complexity of hardware implementation while ensuring ease of understanding and practicality.

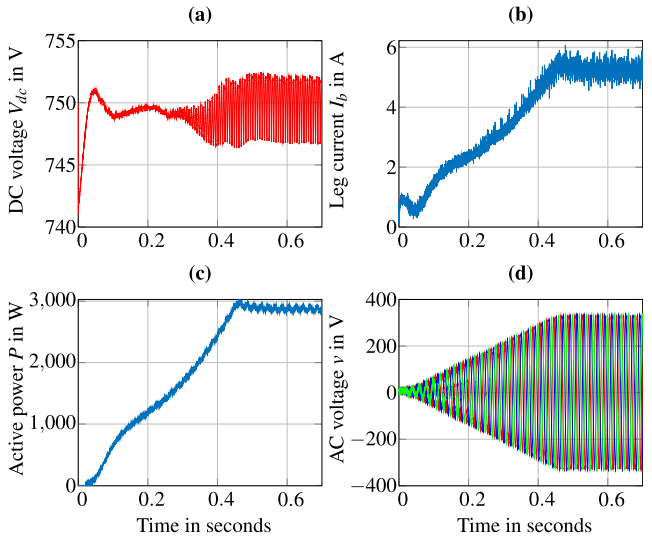

FIGURE 7 | Averaged DC voltage V_{dc} in (a), DC/DC leg inductance current I_b in (b), active power P in (c) and AC voltage v in (d) in the black start experiment.

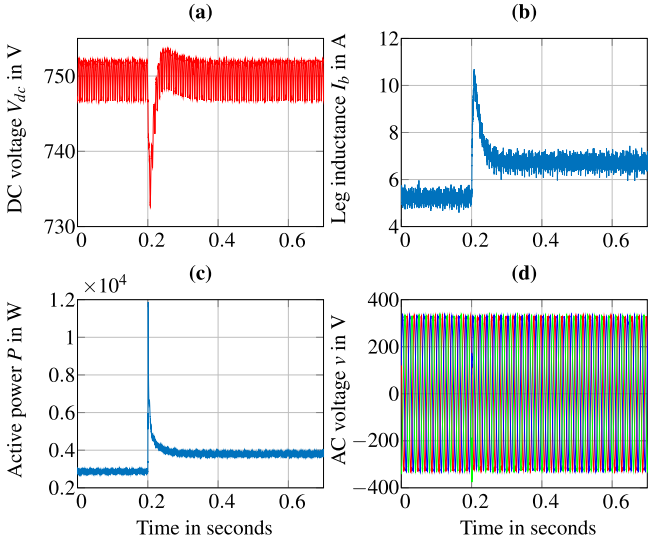

FIGURE 8 | Averaged DC voltage V_{dc} in (a), DC/DC leg inductance current I_b in (b), active power P in (c) and AC voltage v in (d) in the load step experiment.

2.7 | Experimental Results

In the following, we present our main observations from the experiments of Scenario I. All units are in S.I.

2.7.1 | Black Start Capabilities

From Figure 7, we observe that the DC capacitor voltage V_{dc} reaches its nominal value $V_{dc}^{nom} = 750$ within 0.4 s following initial transients. This corresponds to the leg inductance current converging to the steady state value $I_b^s \approx 5$. Following the transients, the visible voltage ripple is due to the sizing of the DC-link capacitors and remains within an acceptable range for the given resistive load. On the AC side, the active power converges to its nominal value $P^* = 2880$ which corresponds to a sinusoidal balanced three-phase signal of the output capacitor voltage v with nominal amplitude $V^d = 230\sqrt{2}$. In essence, Figure 12 shows that both the angle and frequency error converge to zero, that is, the AC frequency and the phase angle of the modulation signal are at their nominal values, namely $\omega^* = 2\pi\,50$ and $\theta^*(t) = 2\pi\,50\,t$, respectively. Thus, our results demonstrate that, even if we start from initial operating conditions far away from nominal operation, resulting from large disturbances, for example, a black start, the angular droop control is able to form sine waves rotating at a nominal frequency with desired angle and amplitude and is therefore grid-forming.

2.7.2 | Step in the Load Power

Proceeding from the steady state after the black start, we study a load step change at $t = 0.2$ s. The active power overshoots to approximately $1.2 \cdot 10^4$ and settles to a new steady state $P^s \approx 3800$, see Figure 8. The overshoot is caused by large rush currents accompanying the change in load power. The DC voltage V_{dc} returns to its nominal value after 0.1 s due to the integral control

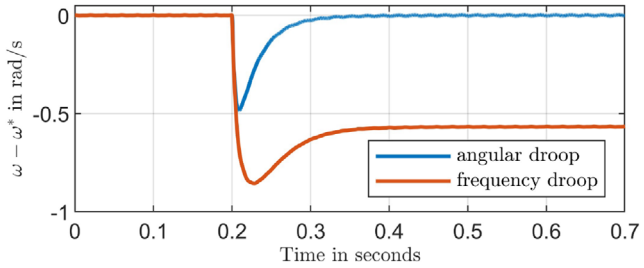

FIGURE 9 | Comparison of angular droop and frequency droop for the load step experiment. Angular droop control uses $\alpha = 2000$, $\gamma = 5 \cdot 10^4$ and frequency control a 5% droop constant.

action of the DC voltage controller, whereby the DC/DC leg inductance current reaches a newly induced steady state $I_b^s \approx 7$ following the load step. The three-phase voltage amplitude drops slightly during the event and recovers to its nominal value at steady state. Figure 13 shows a drop in the AC frequency during the load power change, however the frequency returns to its nominal steady state despite the increase in load power. This zero steady state frequency error is an advantageous, intrinsic property of angular droop control as previously discussed in Section 2.2 and makes the deployment of secondary control to restore the frequency to its nominal value obsolete. Whereas, in a frequency droop controlled setup such a step in the load power causes permanent frequency deviation, unless the power reference is adapted by the secondary control layer. This is shown in Figure 9, where angular droop is compared to frequency droop upon a load step. Note that the steady state deviation for the frequency droop depends on the chosen droop constant.

In the following, we determine a suitable tuning of the angular droop control by studying the influence of the control gains $\alpha, \gamma > 0$ on the frequency and angle of the modulation signal following a step in the load at $t = 0.2$ s. As depicted in Figure 10, an increase in α leads to a higher penalty on the angle and power deviations from their steady state. This translates into a larger rate of change

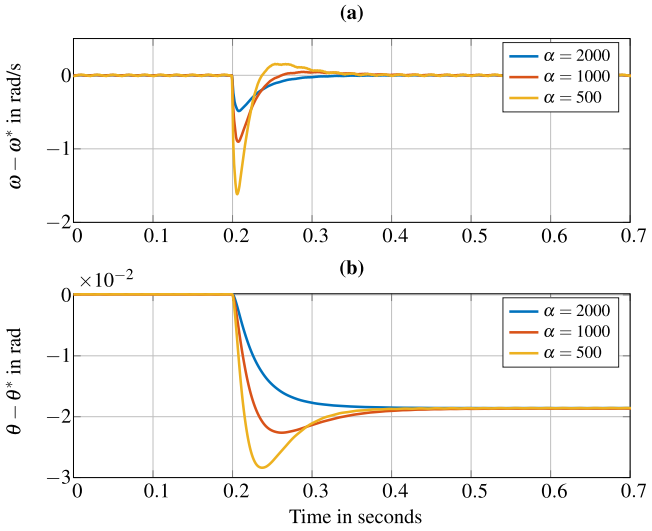

FIGURE 10 | Frequency (a) and angle errors (b) with $\gamma = 5 \cdot 10^4$ and different values for $\alpha \in \{500, 1000, 2000\}$ in the load step experiment.

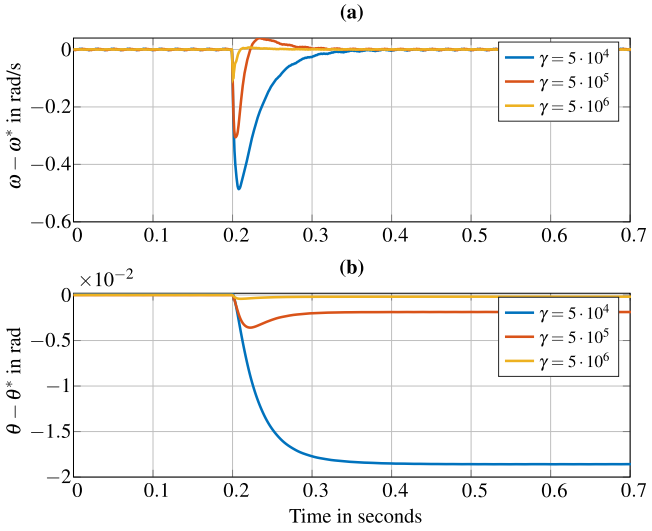

FIGURE 11 | Frequency (a) and angle errors (b) with $\alpha = 2000$ and different values for $\gamma \in \{5 \cdot 10^4, 5 \cdot 10^5, 5 \cdot 10^6\}$ in the load step experiment.

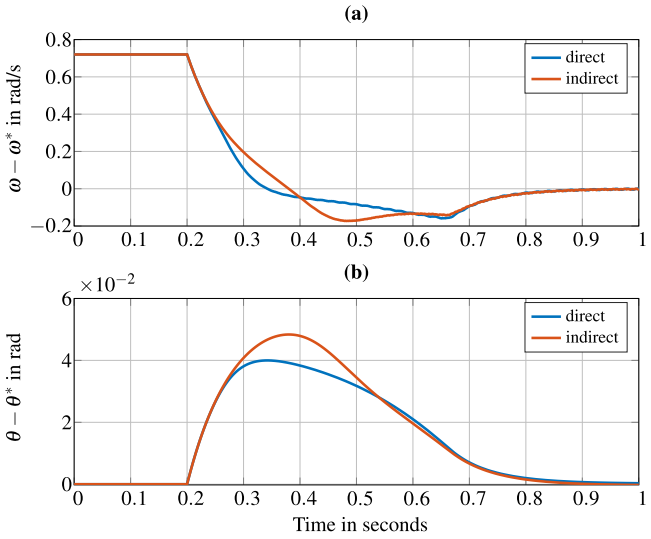

FIGURE 12 | Frequency (a) and angle errors (b) for the black start experiment.

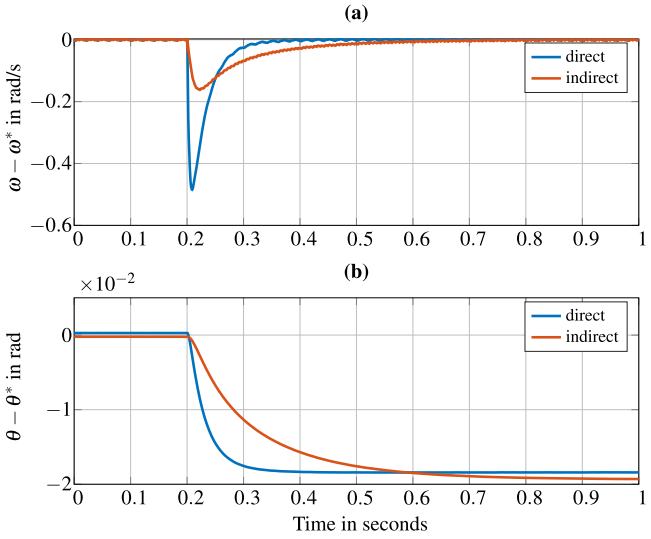

FIGURE 13 | Frequency (a) and angle errors (b) in the load step experiment.

of frequency and smaller nadir. This is in accordance with the observation that, the choice of the gain α affects the transient behavior of the AC frequency ω and angle θ in (6). To avoid an overshoot and limit the frequency deviation to an acceptable deviation of, for example, 0.8 Hz [32], we fix the value $\alpha = 2000$. Figure 11 shows that, for decreasing values of γ the power-to-angle droop behavior is more pronounced resulting in larger steady state angle deviations, see (8). The induced steady state angle θ^s is given by

$$\theta^s = \theta^* + \frac{1}{\gamma}(P^* - P^s), \tag{16}$$

where P^s is the load power at induced steady state following a step in the load. For different γ values the rate of change of the angles during the transient leads to frequency behavior described by (6). This empirically confirms that γ affects both the transients of the AC frequency ω and steady state behavior of the angle θ. Since the choice of $\gamma \geq 5 \cdot 10^5$ leads to relatively small power-to-angle droop behavior, we select $\gamma = 5 \cdot 10^4$.

2.7.3 | Comparison Between Direct and Indirect Control

For the hardware implementation, the angle dynamics resulting from the angular droop control can be translated to a modulation input $\bar{u}$ either directly (direct control) or via well-known cascaded voltage and current control (indirect control). For more details see Appendix A. For the control gains $\alpha = 2000$ and $\gamma = 5 \cdot 10^4$, Figures 12 and 13 compare the frequency and angle errors resulting from the direct and indirect implementation for the black start and the load step experiment, respectively. In Table 2 numerical values for the comparison are presented. Using the indirect implementation, the frequency is restored to its nominal

TABLE 2 | Comparison between direct and indirect control. RMS denotes the root mean square, nadir the smallest value, max. the maximum value and T_{set} the settling time to ±0.02Hz frequency deviation following the event.

Black start experiment					
Control	**Nadir $\Delta\omega$**	**RMS $\Delta\omega$**	**Max. $\lvert\Delta\theta\rvert$**	**RMS $\Delta\theta$**	**T_{set}**
Direct	−0.159	0.165	0.04	0.024	0.61
Indirect	−0.173	0.181	0.48	0.027	0.61
Load step experiment					
Control	**Nadir $\Delta\omega$**	**RMS $\Delta\omega$**	**Max. $\lvert\Delta\theta\rvert$**	**RMS $\Delta\theta$**	**T_{set}**
Direct	−0.485	0.082	0.018	0.0178	0.11
Indirect	−0.162	0.045	0.019	0.0170	0.24

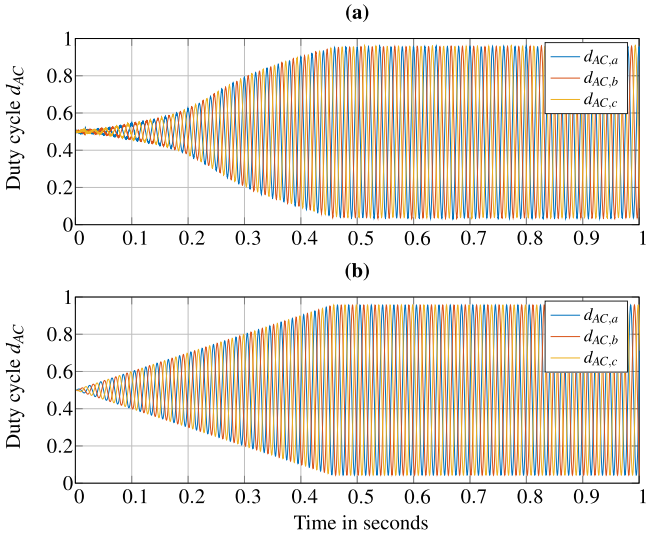

FIGURE 14 | Duty cycles d_{AC} of the indirect (a) and direct control (b) schemes in the black start experiment.

value within approximately 0.61 s and the angles converge to an induced steady state angle θ^s as in Equation (16). In fact, the major difference between direct and indirect control is in the way the control law (A3) relates to the modulation signal representing the main input to the DC/AC converter. In the direct implementation, we assign a sinusoidal wave whose angle is directly determined by the angular droop control. The indirect implementation consists of cascaded voltage and current control loops relying on tracking a given AC voltage reference, whose angle is described by the angular droop control. This results in different modulation signals $\bar{u}$, where the control effort solely dependent on the gains α and γ in the direct scheme. For the indirect scheme, the control effort is also dependent on the choice of the current and voltage control loops, see Table 1. This is visible from the duty cycles d_{AC} in Figure 14, defined by (A2). The duty cycle increases linearly in the direct whereas sub-linearly in the indirect implementation scheme. For our particular control gain choice, this results in a slower convergence rate to a steady state compared to the direct scheme for the load step experiment, see Table 2. Due to its simpler and more intuitive tuning, we adopt the direct implementation of the angular droop control with $\alpha = 2000$ and $\gamma = 5 \cdot 10^4$ in the remainder of our hardware experiments.

3 | Scenario II: Two Identical Converters to a Common Load

The use of angles instead of frequency has further implications for the real-world application of angular droop in grids with multiple converters. Unlike nominal frequency, which is constant, the nominal angle changes over time. This must be considered for the parallel operation of distributed DC/AC converters controlled by angular droop.

3.1 | Scenario Description

Scenario II consists of two identical DC/AC converter systems supplied by two independent DC sources behind DC/DC converters and connected to a common resistive load as shown in Figure 15. Table 1 summarizes the parameter values of the transmission line replicas. To satisfy the modeling assumption of highly inductive transmission lines, we set the ratio $X/R_\ell \approx 11$ with the reactance $X = \omega^* L_\ell$, see also [18]. In this scenario, we verify:

- frequency synchronization capabilities of the angular droop control.
- power-sharing capabilities in dependence of the angular droop control gains.

We hereby underscore the relevance of the two-converter test case as a toy example that provides a solid foundation for generalizations towards n-converter system with $n > 2$ for the following reasons. First, frequency synchronization and power-sharing are fundamental properties that are shared by a network of converter of any size $n > 1$. Second, any analysis comprising n-converters with $n > 2$ can be divided into a pairwise study of two converter i and j and therefore reduces to a two-converter setup. Third, the same implementation challenges, in particular, *clock drifts* are encountered in any extension to a network.

3.2 | Challenge: Clock Drift in Angular Droop Controlled Grids

3.2.1 | Analysis

Angular droop control is susceptible to clock drifts. This is well-documented in the power system literature [18, 33] and can be explained as follows. Let $t_k > 0$ denote the local time at the k-

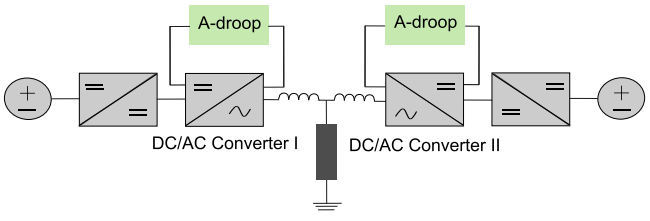

FIGURE 15 | Schematic representation of Scenario II consisting in two identical converter systems, each in closed-loop with angular droop control, connected to a common resistive load via highly inductive transmission lines.

th DC/AC converter with respect to a global reference time t as follows,

$$t_k := (1+\epsilon_k)t, \tag{17}$$

where $\epsilon_k > 0$ is the time-invariant drift of the local clock with respect to the reference clock. This drift arises in the absence of a master clock. Starting from a nominal global frequency $\dot{\theta}_k^s = \omega^*$, the angle obtained from the integration (assuming zero initial conditions) is affected by the clock drift because

$$\theta_k^s(t) = \omega^* t_k = \omega^* (1+\epsilon_k) t = \omega_k t, \tag{18}$$

where $\omega_k := \omega^*(1+\epsilon_k)$ is local frequency at the k-th converter. Under the assumption of a highly inductive, Kron-reduced [34] power network, the active power at the output of the k-th converter at steady state is given by [23]

$$P_k^s = \frac{V_k V_j}{X_{kj}} \sin(\theta_k^s - \theta_j^s) = \frac{V_k V_j}{X_{kj}} \sin((\omega_k - \omega_j)t) \tag{19}$$

$$= \frac{V_k V_j}{X_{kj}} \sin(\omega^* t\,(\epsilon_k - \epsilon_j)), \tag{20}$$

where $\theta_j^s(t) := \omega_j t$ is the steady state angle, ω_j is the local frequency at the j-th converter and X_{jk} is the reactance between converters k and j following Kron-reduction. It can be deduced that when local clock drifts are not compensated for, the injected active power P_k^s drifts apart from its nominal value. Since the angular droop control law involves an integration, the closed-loop dynamics (3) are not robust to local clock drifts [33] and suitable solution needs to be developed for the hardware implementation.

3.2.2 | Proposed Solution

In our lab experiments, we utilize the distribution of a common high-frequency clock [35] (or master clock) across the entire control network through a direct optical fiber connection between the controllers of Converter I and II [36]. Therefore, the distributed devices belong to same clock domain, which eliminates the clock drift for the integration actions. Our proposed solution enables a simple yet resource-friendly realization of angular droop control for testing multi-converter cases and provides a synchronization accuracy of ±2ns [35], surpassing the clock accuracy of the global positioning system (GPS), which is in the range of ±10 ns to ±100 ns [36].

3.3 | Experimental Results

3.3.1 | Frequency Synchronization

Figure 16 depicts the frequency and angle errors following the connection of Converter I and Converter II. Before the interconnection, the modulation angle of Converter I is initialized at zero with $\theta_1^*(t) = \omega^* t$, for $t < 0$ and $\theta_1^*(t) = \omega^* t + \theta_1^*(0)$, for $t \geq 0$. The nominal angle of Converter II is given by $\theta_2^*(t) = \omega^* t + \theta_2^*(0)$, $t \geq 0$, where $\theta_1^*(0)$ and $\theta_2^*(0)$ are the initial angle of Converters I and II at the time of interconnection $t = 0$. The choice of the initial angle $\theta_2^*(0)$ can be determined as follows. The two-converter system

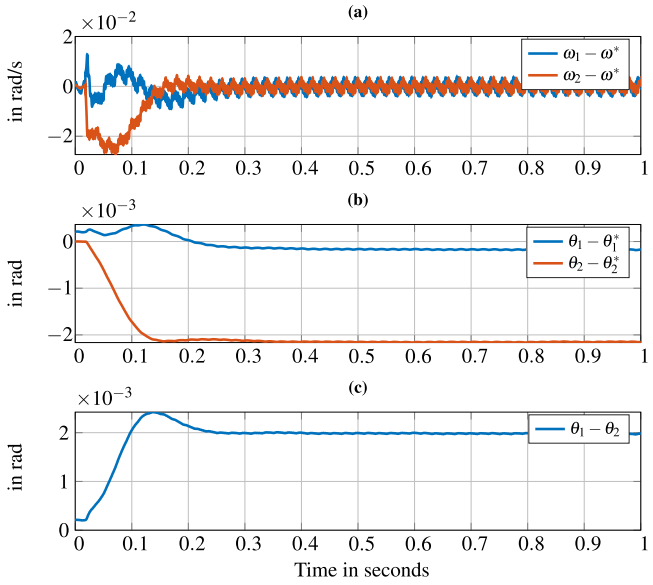

FIGURE 16 | Frequency (a) and angle error (b) for $k = 1, 2$ and angle differences (c), following the connection of Converter II to Converter I at $t = 0$, both in closed-loop with the direct angular droop control for $\gamma_k = 5 \cdot 10^4$ and $\alpha_k = 2000$ for $k = 1, 2$. Here $\theta_1^*(t) = \omega^* t$ for $t < 0$ and $\theta_2^*(t) = \omega^* t + \theta_2^*(0)$ for $t \geq 0$, where $\theta_1(0)$ is the modulation angle of Converter I at the time of interconnection.

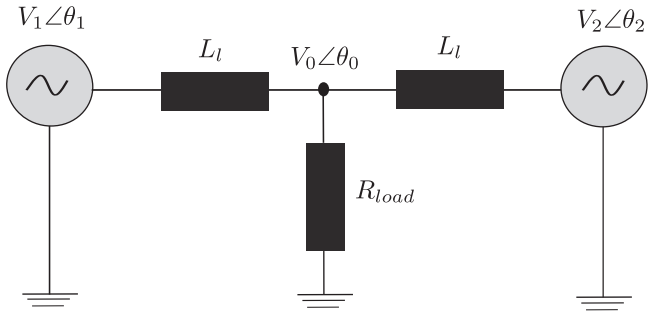

FIGURE 17 | Representation of Scenario II as two voltage sources with switching voltage amplitude V_k and modulation angle θ_k for $k = 1, 2$ supplying a common resistive load under the assumption of a high X/R_l ratio with line reactance $X = \omega^* L_l$ and constant voltage amplitudes.

represented in Figure 15 can be reduced to two sources connected to one load as depicted in Figure 17.

The active power at the k-th DC/AC converter at steady state is given by [23]

$$P_k^s = \frac{V_k V_0}{X_{k0}} \sin(\theta_k^s - \theta_0^s),\ k = \{1, 2\} \tag{21}$$

where $V_0\angle\theta_0^s$ is the phasor at the common node connecting the two converters and $V_k\angle\theta_k^s$ that of the switching voltage of the k-th DC/AC converter with $V_k = \|\frac{1}{2} u_k V_{dc}\|$ and $X_{k0} = \omega^* L_l > 0$ is the reactance of the inductive line impedance. Thus, the active power at Converter II is given by $P_2^s = \frac{V_2 V_0}{X_{20}} \sin(\theta_2^s - \theta_0^s)$. Setting $P_2^s = P_2^* = 0$ leads to $\theta_2^*(0) = \theta_0(0)$. From $P_1^s = \frac{V_1 V_0}{X_{10}} \sin(\theta_1^s - \theta_0^s) =$

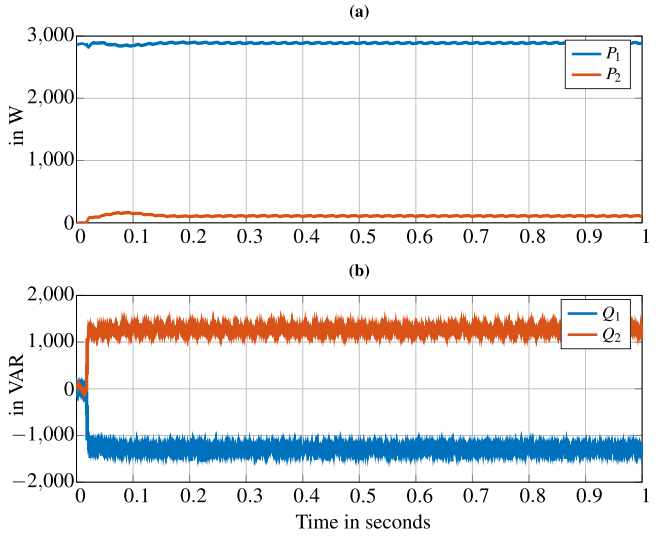

FIGURE 18 | Active (a) and reactive (b) power $P_k^s = v_k^\top i_{o,k}$ and $Q_k^s = v_k^\top \mathbf{J}\, i_{o,k}$ with $P_1^* = P^*, P_2^* = 0$ with $k = 1, 2$ for the frequency synchronization experiment. Converter I and II in closed loop with direct angular droop with $\gamma_k = 5 \cdot 10^4$ and $\alpha_k = 2000$ and $k = 1, 2$.

P^*, we obtain

$$\theta_1^*(0) = \theta_0(0) + \arcsin\left(\frac{P^* X_{10}}{V_0 V_1}\right), \tag{22}$$

where $\arcsin(\frac{P^* X_{10}}{V_0 V_1}) = 0.006$, $\theta_1(0)$ is the initial angle of Converter I and $\theta_0(0)$ is the initial angle at node 0 depicted in Figure 17 obtained from a phased-locked-loop (PLL) scheme at the time of interconnection.

Our experimental results in Figure 16 show that the modulation angle differences at steady state, that is, $\theta_1^s - \theta_2^s = 0.002$. This can be inferred as follows

$$\theta_1^s - \theta_2^s = \theta_1^* - \theta_2^* + \frac{1}{\gamma}(\delta P_1 + \delta P_2) \tag{23}$$

$$= \theta_1(0) - \theta_0(0) + \frac{1}{\gamma}(\delta P_1 + \delta P_2) \tag{24}$$

$$= \theta_0(0) + \arcsin\left(\frac{P^* X_{10}}{V_0 V_1}\right) - \theta_0(0) + \frac{1}{\gamma}(\delta P_1 + \delta P_2) \tag{25}$$

$$= 0.006 + \frac{1}{\gamma}(\delta P_1 + \delta P_2), \tag{26}$$

where $\delta P_1 + \delta P_2 = -200$ and $\delta P_1 = P_1^* - P_1^s$ and $\delta P_2 = P_2^* - P_2^s$. Thereby, the steady state angle differences remain within $[-\pi/2, \pi/2]$ (rad) and the security constraint in [15] is satisfied and the two converters synchronize at nominal frequency ω^* within 0.25 s. Both converters' angles converge to their frequency synchronous steady states. This corresponds to the active power of Converter I and II, P_1^s, P_2^s reaching a nearby nominal value as seen in Figure 18. We note thereby that $P_1^* + P_2^* = P^*$ where P^* is the total active power drawn by the load resistance. Furthermore, the converters exchange reactive power $\tilde{Q}_1^s < 0$ and $\tilde{Q}_2^s > 0$, where $\tilde{Q}_1^s + \tilde{Q}_2^s = 0$ at all times $t \geq 0$. In particular, in a highly inductive, Kron-reduced [34] power network, the reactive power

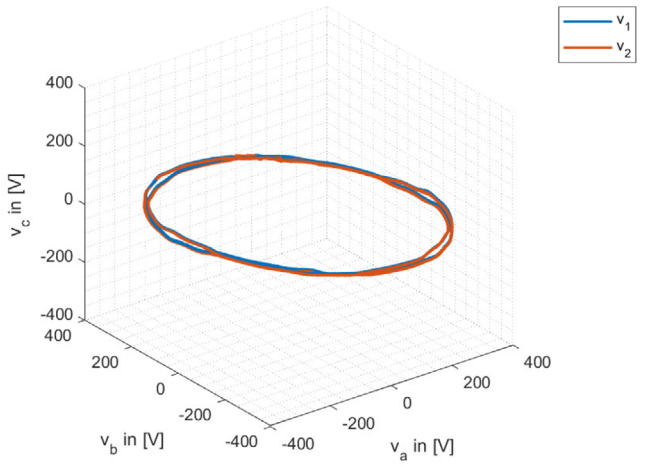

FIGURE 19 | Phase portrait of the periodic orbit of the three-phase output voltages v_1 and v_2 in abc- frame, respectively, in closed-loop with the direct angular droop control for $\gamma_k = 5 \cdot 10^4$ and $\alpha_k = 2000$ and $k = 1, 2$ during the frequency synchronization experiment.

is expressed at the k-th converter by [23]

$$\tilde{Q}_k^s = \frac{V_k}{X_{kj}}(V_k - V_j \cos(\theta_k - \theta_j)), \tag{27}$$

where $k \neq j$ and $k = \{1, 2\}$. Under the small signal approximation, that is, $\theta_k - \theta_j \approx 0$, we obtain

$$\tilde{Q}_k^s \approx \frac{V_k}{X_{kj}}(V_k - V_j). \tag{28}$$

Hence, mismatches of the voltage amplitudes, $V_k \neq V_j$ (see also Figure 19) lead to non-zero reactive power $\tilde{Q}_k^s \neq 0$ for $k = \{1, 2\}$. Such mismatches are unavoidable in hardware setups due to manufacturing tolerances of the used components and parasitic effects that occur in real-world applications. Finally, the phase portrait of the output voltages v_1 and v_2 in Figure 19 represents a limit cycle of an approximate radius of V^d in the phase plane which shows once again the frequency synchronization in AC voltages nearby a desired voltage amplitude V^d. As a conclusion, our experiment validates local asymptotic stability result shown in [15].

3.3.2 | Power-Sharing

To achieve power-sharing among the Converters I and II, we first determine a suitable tuning for the power-to-angle droop gains γ_k, $k = 1, 2$ and the nominal power ratio P_1^*/P_2^*, by conducting the following analysis inspired by [18]. To keep the analysis tractable, we assume in the remainder an inductive power network characterized by high X/R_l ratio (see Table 1), constant voltage magnitudes and neglect the output filter at each converter.

3.3.2.1 | Choice of (γ_k, P_k^*), $k = 1, 2$. Under the small signal approximation, (21) can be rewritten as

$$(\theta_k^s - \theta_0^s) \approx \frac{X_{k0}}{V_k V_0} P_k^s. \tag{29}$$

At steady state, the angular droop control law is given by (8), where

$$\theta_k^s = \theta_k^* + \frac{1}{\gamma_k}(P_k^* - P_k^s), \quad k = 1, 2. \tag{30}$$

Here $\theta_k^s \in \mathbb{R}$ and $P_k^s > 0$ are the induced Kron-reduced steady state angle and active power at the k-th converter.

By letting $\theta_1^s - \theta_2^s = \theta_1^s - \theta_0^s + \theta_0^s - \theta_2^s$, we obtain,

$$\theta_1^* - \theta_2^* - \frac{1}{\gamma_1}(P_1^s - P_1^*) + \frac{1}{\gamma_2}(P_2^s - P_2^*) = \frac{X_{10}}{V_1 V_0}P_1^s - \frac{X_{20}}{V_2 V_0}P_2^s. \tag{31}$$

By reordering the terms in (31), we arrive at

$$\theta_1^* - \theta_2^* + \frac{1}{\gamma_1}P_1^* - \frac{1}{\gamma_2}P_2^* = \left(\frac{1}{\gamma_1} + \frac{X_{10}}{V_1 V_0}\right)P_1^s - \left(\frac{1}{\gamma_2} + \frac{X_{20}}{V_2 V_0}\right)P_2^s. \tag{32}$$

From (22), we have that $\theta_1^*(t) - \theta_2^*(t) = \theta_1(0) - \theta_0(0) = 0.006$. Therefore, if we select the power-to-angle-droop gain $\gamma_k > 0$ such that,

$$\gamma_k \ll \frac{V_k V_0}{X_{k0}}, \quad k = 1, 2 \tag{33}$$

holds, it yields that $\frac{1}{\gamma_1}P_1^* - \frac{1}{\gamma_2}P_2^* \approx \frac{1}{\gamma_1}P_1^s - \frac{1}{\gamma_2}P_2^s$, and we deduce that for an active power ratio defined by,

$$r := \frac{P_1^*}{P_2^*} = \frac{\gamma_1}{\gamma_2}. \tag{34}$$

Therefore, $\frac{P_1^s}{P_2^s} \approx r$ and the power-sharing between the two converters is guaranteed. Finally, for our experimental setup, the condition (33) can be rewritten as

$$\gamma_k \ll 4.8 \cdot 10^5, \tag{35}$$

with $V_1 = V_2 = V^d, V_0 \approx V^d$ and $X_{10} = X_{20} = \omega^* L_l$. To achieve (35), we select $\gamma_1 = \gamma_2 = 500$ with $r = 1$ throughout the power-sharing experiment.

3.3.2.2 | Discussion. Figure 20 shows the experimental results of the power-sharing experiment. The security constraint in [15] is here again satisfied with $\|\theta_1^s - \theta_2^s\| < 0.1$. For $\gamma_1 = \gamma_2 = 500$, power-sharing is guaranteed at steady state, where $P_k^s \approx P^*/2$ for $k = 1, 2$. This corresponds to zero reactive power at steady state. As expected, the two converters synchronize in frequency and their angles converge, respectively, to frequency synchronous steady states within 0.5 s. Thus, our experiment validates the power-sharing capabilities of the angular-droop controlled DC/AC converter system, one of the most important plug and play properties for converter control design in power networks.

4 | Conclusion

We demonstrate the grid-forming properties of the angular droop control in two scenarios embedded in a hardware experiment

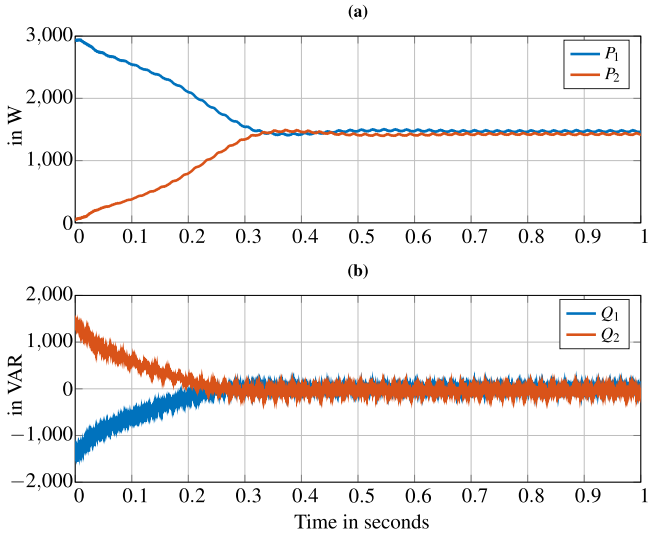

FIGURE 20 | Active power $P_k = v_k^\top i_{o,k}$ in (a) and reactive power $Q_k = v_k^\top \mathbf{J} i_{o,k}$ in (b) following the connection of Converter II to Converter I at $t = 0$, both in closed-loop with the direct angular droop control for $\gamma_k = 500, \alpha_k = 2000$ and the power ratio $r = 1$ in (34) for $k = 1, 2$ in the power-sharing experiment, $P_1^* = P_2^* = \frac{P^*}{2}$.

setup. For this we provide traceable analysis and solutions to the challenges that arise from virtual angle control in real-world applications. First, the discretized control law is rewritten to conform with the restrictions posed by hardware implementation. Second, the susceptibility to clock drifts in multi-converter settings is analyzed and resolved by distributing a common master clock. Using a single converter setup, the black start capabilities of angular droop control as well as the capability to withstand sudden load changes while returning to zero frequency deviation is shown. With the extension to a multi-converter setup the frequency synchronization as well as load sharing properties are demonstrated and tuning guidelines are established. Our future work aims to extend the angular droop control with voltage regulation, therefore relaxing the assumption on constant AC voltage amplitude. Furthermore, the interoperability of angular droop with other control strategies needs to be considered. For prospective industrial-microgrid applications, the influence of nonlinear loads as well as the extension to larger multi-converter setup will be investigated.

Author Contributions

Taouba Jouini: conceptualization, data curation, formal analysis, investigation, methodology, visualization, writing – original draft, writing – review & editing. **Jan Wachter:** conceptualization, data curation, formal analysis, investigation, methodology, visualization, writing – original draft, writing – review & editing. **Sophie An:** conceptualization, formal analysis, investigation, methodology, writing – original draft. **Veit Hagenmeyer:** conceptualization, funding acquisition, supervision, writing – review & editing.

Acknowledgements

We acknowledge support by the KIT Publication Fund of the Karlsruhe Institute of Technology.

Open access funding enabled and organized by Projekt DEAL.

Funding

The authors have nothing to report.

Conflicts of Interest

The authors declare no conflicts of interest.

Data Availability Statement

The data that support the findings of this study are available from the corresponding author upon reasonable request.

References

1. A. Sajadi, J. A. Rañola, R. W. Kenyon, B.-M. Hodge, and B. Mather, "Dynamics and Stability of Power Systems With High Shares of Grid-Following Inverter-Based Resources: A Tutorial," *IEEE Access* 11 (2023): 29591–29613, https://doi.org/10.1109/ACCESS.2023.3260778.

2. J. Wachter, L. Gröll, and V. Hagenmeyer, "Survey of Real-World Grid Incidents–Opportunities, Arising Challenges and Lessons Learned for the Future Converter Dominated Power System," *IEEE Open Journal of Power Electronics* 5 (2024): 50–69, https://doi.org/10.1109/OJPEL.2023.3343167.

3. F. Dörfler and D. Groß, "Control of Low-Inertia Power Systems," *Annual Review of Control, Robotics, and Autonomous Systems* 6, no. 1 (May 2023): 415–445, https://doi.org/10.1146/annurev-control-052622-032657.

4. J. W. Simpson-Porco, F. Dörfler, and F. Bullo, "Synchronization and Power Sharing for Droop-Controlled Inverters in Islanded Microgrids," *Automatica* 49, no. 9 (2013): 2603–2611, https://doi.org/10.1016/j.automatica.2013.05.018.

5. S. Chakraborty, S. Patel, G. Saraswat, A. Maqsood, and M. V. Salapaka, "Seamless Transition of Critical Infrastructures Using Droop-Controlled Grid-Forming Inverters," *IEEE Transactions on Industrial Electronics* 71, no. 2 (Feb. 2024): 1535–1546, https://doi.org/10.1109/TIE.2023.3253946.

6. T. Jouini, C. Arghir, and F. Dörfler, "Grid-Friendly Matching of Synchronous Machines by Tapping Into the DC Storage," *IFAC-PapersOnLine* 49, no. 22 (2016): 192–197, https://doi.org/10.1016/j.ifacol.2016.10.395.

7. C. Arghir, T. Jouini, and F. Dörfler, "Grid-Forming Control for Power Converters Based on Matching of Synchronous Machines," *Automatica* 95 (2018): 273–282, https://doi.org/10.1016/j.automatica.2018.05.037.

8. B. B. Johnson, S. V. Dhople, A. O. Hamadeh, and P. T. Krein, "Synchronization of Parallel Single-Phase Inverters With Virtual Oscillator Control," *IEEE Transactions on Power Electronics* 29, no. 11 (2014): 6124–6138, https://doi.org/10.1109/TPEL.2013.2296292.

9. B. B. Johnson, M. Sinha, N. G. Ainsworth, F. Dörfler, and S. V. Dhople, "Synthesizing Virtual Oscillators to Control Islanded Inverters," *IEEE Transactions on Power Electronics* 31, no. 8 (2015): 6002–6015.

10. M. Sinha, F. Dörfler, B. B. Johnson, and S. V. Dhople, "Virtual Oscillator Control Subsumes Droop Control," in *2015 American Control Conference (ACC)* (IEEE, 2015), 2353–2358, https://doi.org/10.1109/ACC.2015.7171084.

11. M. Colombino, D. Groß, J.-S. Brouillon, and F. Dörfler, "Global Phase and Magnitude Synchronization of Coupled Oscillators With Application to the Control of Grid-Forming Power Inverters," *IEEE Transactions on Automatic Control* 64, no. 11 (2019): 4496–4511, https://doi.org/10.1109/TAC.2019.2898549.

12. G.-S. Seo, M. Colombino, I. Subotic, B. Johnson, D. Groß, and F. Dörfler, "Dispatchable Virtual Oscillator Control for Decentralized Inverter-Dominated Power Systems: Analysis and Experiments," in *2019 IEEE Applied Power Electronics Conference and Exposition (APEC)* (IEEE, 2019), 561–566.

13. R. Strunk, P. Sourkounis, and A. Mertens, "Impedance-Based Stability Analysis of Grid-Forming Inverters With Virtual Impedance or Angle Droop for Improved Robustness," in *2024 IEEE 15th International Symposium on Power Electronics for Distributed Generation Systems (PEDG)* (IEEE, 2024), 1–6, https://doi.org/10.1109/PEDG61800.2024.10667448.

14. R. Majumder, A. Ghosh, G. Ledwich, and F. Zare, "Angle Droop Versus Frequency Droop in a Voltage Source Converter Based Autonomous Microgrid," in *2009 IEEE Power & Energy Society General Meeting* (IEEE, 2009), 1–8.

15. T. Jouini, A. Rantzer, and E. Tegling, "Inverse Optimal Control for Angle Stabilization in Converter-Based Generation," in *2022 American Control Conference (ACC)* (IEEE, 2022), 4945–4950.

16. T. Jouini, "Network Synchronization and Control Based on Inverse Optimality: A Study of Inverter-Based Power Generation," (Doctoral thesis, Department of Automatic Control, 2021).

17. T. Jouini and A. Rantzer, "On Cost Design in Applications of Optimal Control," *IEEE Control Systems Letters* 6 (2022): 452–457, https://doi.org/10.1109/LCSYS.2021.3079642.

18. R. R. Kolluri, I. Mareels, T. Alpcan, M. Brazil, J. de Hoog, and D. A. Thomas, "Power Sharing in Angle Droop Controlled Microgrids," *IEEE Transactions on Power Systems* 32, no. 6 (2017): 4743–4751, https://doi.org/10.1109/TPWRS.2017.2672569.

19. T. Xu, J. Zhou, L. Liang, et al., "Consensus Active Power Sharing for Islanded Microgrids Based on Distributed Angle Droop Control," *IET Renewable Power Generation* 15, no. 13 (2021): 2826–2839, https://doi.org/10.1049/rpg2.12210.

20. T. Jouini, Z. Sun, V. Renganathan, and V. Hagenmeyer, "Input and State Constrained Inverse Optimal Control With Application to Power Networks," *IFAC-PapersOnLine* 56, no. 2 (2023): 5451–5456, https://doi.org/10.1016/j.ifacol.2023.10.196.

21. T. Jouini, Z. Sun, and V. Hagenmeyer, "Tuning of Discrete-Time Angular Droop Controllers," in *2023 IEEE Conference on Control Technology and Applications (CCTA)* (IEEE, 2023), 741–745, https://doi.org/10.1109/CCTA54093.2023.10252209.

22. F. Wiegel, J. Wachter, M. Kyesswa, R. Mikut, S. Waczowicz, and V. Hagenmeyer, "Smart Energy System Control Laboratory – A Fully-Automated and User-Oriented Research Infrastructure for Controlling and Operating Smart Energy Systems," *at-Automatisierungstechnik* 70, no. 12 (2022): 1116–1133.

23. P. Kundur, N. J. Balu, and M. G. Lauby, *Power System Stability and Control*, Vol. 7 (McGraw-Hill, 1994).

24. M. Golshani, D. Wilson, S. Norris, I. Cowan, M. H. Rahman, and B. Marshall, "Application of Phasor-Based Functionality to HVDC Control in Reduced System Strength," in *The 17th International Conference on AC and DC Power Transmission (ACDC 2021)* 2021 (IEEE, 2021), 44–49, https://doi.org/10.1049/icp.2021.2442.

25. T. Wang, J. Yang, M. Padhee, J. Bi, A. Pal, and Z. Wang, "Robust, Coordinated Control of SSO in Wind-Integrated Power System," *IET Renewable Power Generation* 14, no. 6 (2020): 1031–1043, https://doi.org/10.1049/ietrpg.2019.0410.

26. D. Fank and H. Renner, "Deployment of a Full-Size Converter Utilised Hydropower Plant to Enhance Inter-Area Oscillation Damping," *IET Generation, Transmission & Distribution* 18, no. 10 (2024): 1992–2005, https://doi.org/10.1049/gtd2.13165.

27. Imperix, Half-Bridge SiC Power Module, rev.C/(March 2021), https://imperix.com/wp-content/uploads/document/PEB8038.pdf.

28. Imperix, Passive Filters Box, rev. D/(March, 2021), https://imperix.com/wp-content/uploads/document/Passives_Rack.pdf.

29. Imperix, B-Box RCP Rapid Prototyping Controller, rev. (11/08/21), https://imperix.com/wp-content/uploads/document/B-Box_Datasheet.pdf.

30. Imperix, 50A DIN Rail-Mountable Current Sensor, datasheet, https://imperix.com/wp-content/uploads/document/DIN-50A.pdf.

31. Imperix, 800V DIN Rail-Mountable Voltage Sensor, datasheet, https://imperix.com/wp-content/uploads/document/DIN-800V.pdf.

32. Commission of European Union (EU), "Commission Regulation (EU) 2017/1485 of 2 August 2017 Establishing a Guideline on Electricity

Transmission System Operation," https://eur-lex.europa.eu/legal-content/EN/TXT/?uri=CELEX:02017R1485-20210315.

33. J. Schiffer, C. A. Hans, T. Kral, R. Ortega, and J. Raisch, "Modeling, Analysis, and Experimental Validation of Clock Drift Effects in Low-Inertia Power Systems," *IEEE Transactions on Industrial Electronics* 64, no. 7 (2017): 5942–5951, https://doi.org/10.1109/TIE.2016.2638805.

34. F. Dörfler and F. Bullo, "Kron Reduction of Graphs With Applications to Electrical Networks," *IEEE Transactions on Circuits and Systems I: Regular Papers* 60, no. 1 (2013): 150–163, https://doi.org/10.1109/TCSI.2012.2215780.

35. Imperix, "Real Sync," https://imperix.com/technology/distributed-modulation/.

36. IEEE, "IEC/IEEE International Standard - Precision Clock Synchronization Protocol for Networked Measurement and Control Systems," IEC 61588:2009(E) (2009): 1–292, https://doi.org/10.1109/IEEESTD.2009.4839002.

37. T. Jouini and Z. Sun, "Frequency Synchronization of a High-Order Multiconverter System," *IEEE Transactions on Control of Network Systems* 9, no. 2 (2022): 1006–1016, https://doi.org/10.1109/TCNS.2021.3128493.

Appendix A

A.1 | High-Order Converter Modeling and Control

This section details how the angular droop control law (2) is implemented on the experiment hardware. With some abuse of notation, we omit throughout subsequent sections the subscript k to denote a quantity z_k of the k-th converter.

A.1.1 | Modeling and Control DC/AC Converter. We start by relaxing our modeling assumptions from Section 2 towards a hardware experiment in two directions:

- First, we include a DC power supply and a DC/DC converter relying on vector control consisting of cascaded voltage and current control loops put in series behind the DC/AC converter to provide adequate DC-link voltage.
- Second, even though the derivation of the angular droop control ignores the internal dynamics of the converter, we present a sufficiently detailed, high-order model of the DC/AC converter. Based on it, we suggest a direct and indirect method to implement the angular droop control (2) by modulation control.

Hereby, we further assume that all AC voltage amplitudes are constant and at nominal.

A.1.2 | Modeling DC/AC Converter. We consider a three-phase, averaged and balanced DC/AC converter as shown in Figure 3 and described in abc-frame [23, 37],

$$\begin{aligned} L\,\dot{i} &= -R\,i + \frac{1}{2}\overline{u}\,V_{dc} - v, \\ C\,\dot{v} &= -G\,v + i - i_o, \end{aligned} \tag{A.1}$$

where V_{dc} denotes the DC side capacitor voltage. On the AC side, let $i \in \mathbb{R}^3$ denote the inductance current and $v \in \mathbb{R}^3$ the output voltage. The filter resistance and inductance are specified by $R > 0$ and $L > 0$, respectively. The capacitor $C > 0$ is set in parallel with the load conductance $G > 0$ to ground. The DC/AC converter is connected to the AC network, where $i_o \in \mathbb{R}$ is the output current flowing into the network. Note that the pulse width modulation signal $\overline{u} \in [-1, 1]$ relates to the converter duty cycle $d_{AC} \in [0, 1]$ via

$$d_{AC} = \frac{1}{2} + \frac{\overline{u}}{2}, \tag{A.2}$$

where $\overline{u}$ represents the main input to the DC/AC converter.

A.1.3 | Direct Implementation. First, we define the active power $P = v^\top i_o$, and the nominal steady state $P^* = v^{*\top} i_o^*$. For the direct implementation of the angular droop control we propose

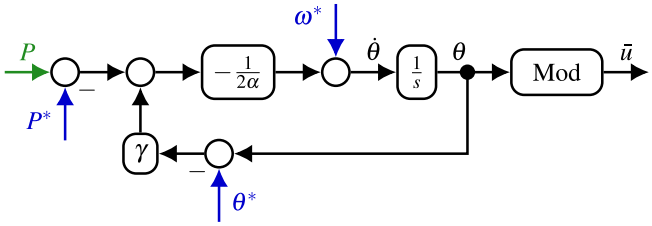

FIGURE A.1 | Implementation of the angular droop for the DC/AC converter via direct control of the modulation signal $\bar{u}$.

$$\dot{\theta} = -\frac{1}{2\alpha}(\gamma(\theta - \theta^*) + (P - P^*)) + \omega^*, \tag{A.3a}$$

$$\overline{u} = A\begin{bmatrix} \sin(\theta) \\ \sin\left(\theta - \frac{2\pi}{3}\right) \\ \sin\left(\theta + \frac{2\pi}{3}\right) \end{bmatrix}, \tag{A.3b}$$

where $0 < A < 1$ is the amplitude of the modulation signal $\overline{u}$. Figure A.1 depicts a summarizing block diagram of the direct implementation of the angular droop control (2). Note that in (A.3), the angular droop control increments the converter's state with a virtual angle θ through the modulation signal $\bar{u}$.

A.1.4 | Indirect Implementation. We propose an indirect implementation of the angular droop control that relies on cascaded control. In particular, the indirect implementation entails inner voltage and current control loop according to a cascaded architecture. After a Park transformation $\mathcal{P}(\theta_{dq})$ with angle $\theta_{dq}(t) := \theta(t)$ and given the reference voltage v^d in abc-frame [23],

$$v^d(\theta) = V^*\begin{bmatrix} \sin(\theta) \\ \sin\left(\theta - \frac{2\pi}{3}\right) \\ \sin\left(\theta + \frac{2\pi}{3}\right) \end{bmatrix}, \tag{A.4}$$

with $V^* > 0$ the reference voltage amplitude and θ the angle given by (3), the tracking of the reference voltage (A.4) is achieved via cascaded voltage and current loops implementing proportional-integral (PI) controllers. Thereby, the outer voltage loop generates a reference current signal

$$i_{dq}^d = Y\,v_{dq} + i_{o,dq} - k_{VP}(v_{dq} - v_{dq}^d) - k_{VI}\int_0^t \left(v_{dq}(\tau) - v_{dq}^d\right)\mathrm{d}\tau, \tag{A.5}$$

where $k_{VP}, k_{VI} > 0$ are the control gains and $Y = G + C\mathbf{J}\omega^*$. To track the reference current (A.5), we design an inner current loop based on PI control using the switching voltage $v_m^d = \frac{1}{2}\overline{u}_{dq}\,V_{dc}$ as follows

$$v_m^d = Z\,i_{dq} + v_{dq} - k_{IP}\left(i_{dq} - i_{dq}^d\right) - k_{II}\int_0^t \left(i_{dq}(\tau) - i_{dq}^d\right)\mathrm{d}\tau, \tag{A.6}$$

where $k_{IP}, k_{II} > 0$ are control gains and $Z = R + L\,\mathbf{J}\,\omega^*$. By applying the inverse Park transformation $\mathcal{P}^{-1}(\theta_{dq})$, we recover the modulation input $\overline{u}$ in abc-frame as follows,

$$\overline{u}(\theta) = 2\,\frac{\mathcal{P}^{-1}(\theta_{dq})\,(v_m^d)}{V_{dc}}. \tag{A.7}$$

It is noteworthy that, the pairs (k_{VP}, k_{VI}) and (k_{IP}, k_{II}) are chosen to guarantee time-scale separation, where the current control loop is faster than the voltage control loop. Figure A.2 summarizes the overall scheme of the indirect implementation based on cascaded control.

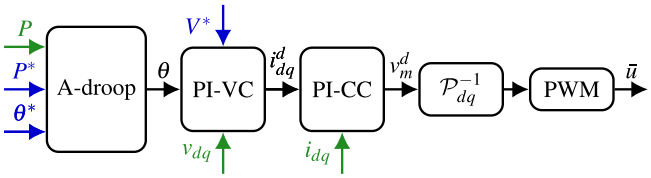

FIGURE A.2 | Indirect cascaded control of the angular droop after dq-transformation of the DC/AC converter. PI-VC and PI-CC denote the proportional integral (PI) voltage and current controller, respectively.

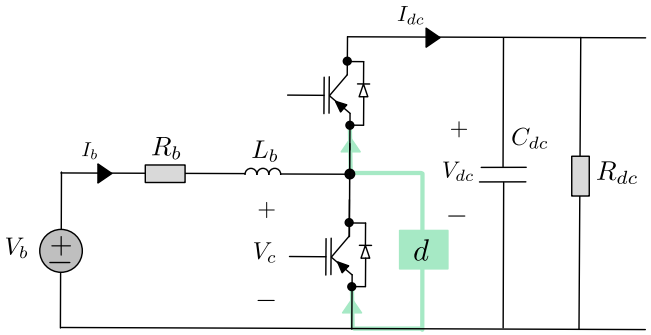

FIGURE A.3 | A schematic representation of the boost converter consisting of a half-bridge module and an inductance L_b with the parasitic resistance R_b.

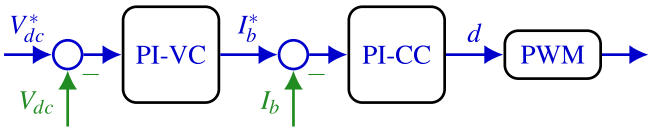

FIGURE A.4 | Summary of the vector control of the boost converter using as main input the duty cycle d in (A.12).

A.2 | Modeling and Control DC/DC Boost Converter

A.2.1 | Modeling DC/DC Boost Converter. Figure A.3 depicts the boost converter in our experimental setup. Observe that the two-switch configuration is due to the available half-bridge modules. However, only the lower switch is actuated to perform the desired control action. The upper switch is actuated complementary to reduce the losses through the parallel diode. The boost converter is modeled by following ordinary differential equations,

$$\begin{aligned} L_b \dot{I}_b &= -R_b I_b + V_b - V_c\,, \\ C_{dc}\dot{V}_{dc} &= -G_{dc}V_{dc} + I_{dc}, \quad I_{dc} = \frac{V_b I_b}{V_{dc}}\,. \end{aligned} \tag{A.8}$$

In (A.8), we denote by $I_b \in \mathbb{R}$ the current flowing out of the DC supply and by V_b the DC supply voltage. The conductance $G_{dc} = 1/R_{dc} > 0$ models the parasitic losses on the DC side. The inductance is represented by L_b and the DC capacitance is given by $C_{dc} > 0$. Additionally, $V_{dc} \in \mathbb{R}$ represents the voltage across the DC capacitor and $V_c \in \mathbb{R}$ is the voltage controlled directly by the duty cycle $d \in [0, 1]$ via the relationship

$$V_c = (1 - d) \cdot V_{dc} \in \mathbb{R}. \tag{A.9}$$

Note that the duty cycle d in (A.9) represents the main control input to the boost converter.

A.2.2 | Boost Converter. The cascaded control architecture to regulate the DC-bus voltage of the boost converter exploits the differential equations (A.8) and is summarized in Figure A.4. In particular, an outer loop regulates the DC capacitor voltage V_{dc} at a nominal value $V_{dc}^* > V_b >$ 0 by specifying a reference current $I_b^d \in \mathbb{R}$ given explicitly by,

$$I_b^d = \frac{V_{dc}}{V_b} \cdot \left(G_{dc}V_{dc} - k_P(V_{dc} - V_{dc}^*) - k_I \int_0^t (V_{dc}(\tau) - V_{dc}^*)\mathrm{d}\tau \right), \tag{A.10}$$

where $k_P > 0$, $k_I > 0$ are proportional and integral control gains. The reference current I_b^d in (A.10) is tracked by an inner current control loop leveraging the reference voltage $V_l^d := V_b - V_c$ as follows,

$$V_l^d = R_b I_b - k_{BP}\left(I_b - I_b^d\right) - k_{BI} \int_0^t \left(I_b(\tau) - I_b^d\right)\mathrm{d}\tau, \tag{A.11}$$

with k_{BP}, $k_{BI} > 0$. The choice of the gain pairs (k_P, k_I) and (k_{BP}, k_{BI}) ensures time-scale separation, namely that the closed-loop dynamics of the current loop is faster than that of DC voltage. Finally, the duty cycle d, that is, the main input to the boost converter is deduced from the reference voltage V_l^d in (A.9) and (A.11) via the relationship,

$$d = 1 - \frac{V_b - V_l^d}{V_{dc}}. \tag{A.12}$$